



Cite this: *J. Mater. Chem. C*, 2015, **3**, 7492

In situ high-energy synchrotron X-ray diffraction revealing precipitation reaction kinetics of silver ions with mixed halide ions†

Qi Liu,^{‡a} Zheng Li,^{‡a} John S. Okasinski,^b Yang Ren^b and Yugang Sun^{*a}

Precipitation of silver ions simultaneously with chloride and bromide ions in ethylene glycol at a mild temperature (e.g., 60 °C) has been successfully demonstrated for the synthesis of silver chlorobromide ($\text{AgCl}_x\text{Br}_{1-x}$, $0 < x < 1$) nanoparticles, which is realized by injecting a AgNO_3 solution into a solution containing both halogen ions. The injection rate of the AgNO_3 solution has been determined to be critical for controlling the uniformity of $\text{AgCl}_x\text{Br}_{1-x}$ nanoparticles. Time-resolved *in situ* high-energy synchrotron X-ray diffraction has been applied, for the first time, to quantitatively monitor the reaction kinetics of nanocrystal formation. The real-time results shed light on the fact that the injection rate of AgNO_3 solution significantly influences the nucleation and growth processes, and thus the quality of resulting $\text{AgCl}_x\text{Br}_{1-x}$ nanoparticles. Specifically, fast injection enables the complete addition of AgNO_3 solution to the reaction solution before the nucleation process starts, leading to a good separation of nucleation and growth and thus the formation of uniform $\text{AgCl}_x\text{Br}_{1-x}$ nanocubes with well-defined composition and narrow size distribution. By contrast, slow injection results in a continuous addition of AgNO_3 solution to the reaction solution even after nucleation starts, leading to continuous multiple nucleation/growth processes and thus the formation of $\text{AgCl}_x\text{Br}_{1-x}$ nanoparticles with broad dimensional and morphological distributions.

Received 8th May 2015,
Accepted 17th June 2015

DOI: 10.1039/c5tc01306b

www.rsc.org/MaterialsC

1 Introduction

Intensive studies have been carried out recently on the synthesis of nanocrystalline silver halides and their derivative composites due to their unique optical properties and excellent photocatalytic activities.^{1–15} Among all kinds of silver halides, silver chlorobromide ($\text{AgCl}_x\text{Br}_{1-x}$, $0 < x < 1$) nanoparticles represent a class of interesting materials that can offer many advantages in comparison with either AgCl or AgBr . For example, the refractive index of $\text{AgCl}_x\text{Br}_{1-x}$ can be tuned by adjusting its chemical composition to make them the promising candidates in interesting applications.^{16–19} The properties of silver halide nanoparticles are usually dependent on their morphology and uniformity (in terms of size, composition, and crystallinity), and therefore controlled synthesis of $\text{AgCl}_x\text{Br}_{1-x}$ nanoparticles with well-defined crystalline structure, size, and morphology is critically important for studying their property–performance relationship.^{20–23} An ion-exchange method

has been reported for the synthesis of photocatalytically active $\text{AgCl}_x\text{Br}_{1-x}$ nanoparticles, which exhibit completely random morphologies and very broad size distribution.²⁴ Most recently we have developed a co-precipitation method, in which Ag^+ ions simultaneously precipitate with both Cl^- and Br^- ions in aqueous solutions containing poly(vinyl pyrrolidone) (PVP) as a stabilizing surfactant, for the synthesis of $\text{AgCl}_x\text{Br}_{1-x}$ nanoparticles with highly pure crystalline phase.²⁵ Similar co-precipitation reactions in microemulsion droplets are also able to produce $\text{AgCl}_x\text{Br}_{1-x}$ nanoparticles with tunable compositions.²⁶ However, the lack of control over reaction kinetics leads to the difficulty in exerting precise control over morphology and size distribution of the synthesized nanoparticles. By replacing aqueous solutions with ethylene glycol solutions with high viscosity that can be tuned by controlling temperature to determine the diffusion rate of ionic species, the nucleation and growth steps involved in the synthesis of $\text{AgCl}_x\text{Br}_{1-x}$ nanoparticles can be well separated under appropriate conditions, leading to the production of $\text{AgCl}_x\text{Br}_{1-x}$ nanocubes with significantly improved uniformity (including morphology, size, composition, and crystallinity).²⁷ Among various reaction conditions, the injection rate of the precursor solution containing Ag^+ ions is found to be the most important parameter to determine the quality of the resulting $\text{AgCl}_x\text{Br}_{1-x}$ nanocubes. Therefore, real-time probing

^a Center for Nanoscale Materials, Argonne National Laboratory, 9700 South Cass Ave, Argonne, Illinois 60439, USA. E-mail: ygsun@anl.gov

^b X-ray Science Division, Advanced Photon Source, Argonne National Laboratory, 9700 South Cass Ave, Argonne, Illinois 60439, USA

† Electronic supplementary information (ESI) available. See DOI: 10.1039/c5tc01306b

‡ These authors contributed equally.

of the reaction kinetics at different injection rates of the precursor solution is critical to better understand the nucleation and growth mechanisms of the co-precipitation reaction as well as to better control and improve the quality of $\text{AgCl}_x\text{Br}_{1-x}$ nanocubes. In our previous work, an *in situ* high-energy synchrotron X-ray diffraction (XRD) technique was used to record the evolution of nanocrystals formed in the reaction solutions.²⁷ The use of high-energy (70 keV) X-ray beams is advantageous for real-time probing nanophase evolution of colloidal nanoparticles in solutions because of their deep penetration into the liquid solutions and weak absorption in the reactants, which can reduce the interference of the background and eliminate the possibility of X-ray-induced side reactions.²⁸ It is still challenging to extract quantitative reaction kinetics from the time-resolved XRD patterns since Rietveld refinement analysis becomes difficult (even impossible) to apply to the convoluted XRD peaks of mixed nanocrystals with continuously varied compositions. In addition, the few number of diffraction peaks of the individual XRD pattern also limits the use of Rietveld refinement for accurate fitting.

In this paper, we report the analysis of the XRD patterns by fitting them with multiple Gaussian functions in OriginLab[®]. The fitting leads to the availability of quantitative data for the precipitation reaction kinetics involved in the formation of $\text{AgCl}_x\text{Br}_{1-x}$ nanoparticles at varying injection rates of the precursor solution. The quantitative analysis reveals that fast injection of the precursor Ag^+ solution is beneficial for the synthesis of uniform $\text{AgCl}_x\text{Br}_{1-x}$ nanocubes with narrow size distribution and pure crystalline phase. Ideally, the precursor Ag^+ solution has to be completely added to the solution containing halogen ions before the $\text{AgCl}_x\text{Br}_{1-x}$ nanocrystals can be detected by *in situ* XRD. In contrast, continuous nucleation and growth occurs when the injection rate of the precursor Ag^+ solution is low, resulting in the formation of a mixture of $\text{AgCl}_x\text{Br}_{1-x}$ nanoparticles with varying morphologies (including cube, sphere, rod, dimer, *etc.*) and two different sets of sizes and compositions.

2 Experimental

Synthesis of silver chlorobromide ($\text{AgCl}_x\text{Br}_{1-x}$) nanocubes was carried out by a co-precipitation reaction as reported in our recent work.²⁷ All chemicals used in the synthesis were used as received without further purification and all the syntheses were done in the dark under the protection of a nitrogen atmosphere. Briefly, 2.5 g of poly(vinyl pyrrolidone) (PVP, $M_w \approx 55\,000$, Sigma-Aldrich), together with 10.227 mg of NaCl (Fisher Chemicals) and 20.825 mg of KBr (Sigma-Aldrich) (the molar ratio of NaCl:KBr is 1:1) were added to 12 mL of ethylene glycol (J. T. Baker) followed by dissolution with the assistance of heating at 60 °C. To this solution, 1 mL of ethylene glycol solution of AgNO_3 (0.34 M, Sigma-Aldrich) was injected at an appropriate constant rate. The reaction solution was continuously heated at 60 °C for 2 hours. The morphology and the size of the synthesized nanoparticles were examined using transmission

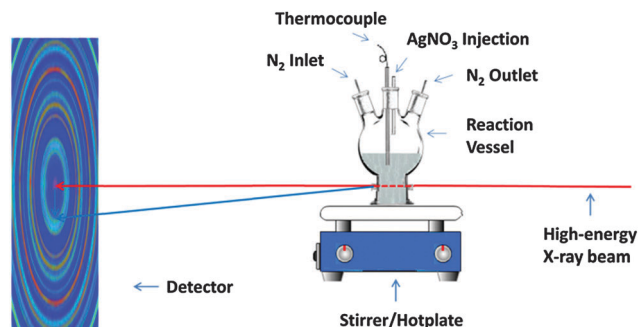


Fig. 1 Schematic illustration of the experimental set-up that was developed for the *in situ* probing of the synthesis of silver chlorobromide nanocrystals.

electron microscopy (JEOL 2100F microscope, operated at an accelerating voltage of 200 kV) and scanning electron microscopy (JEOL JSM-7500F microscope).

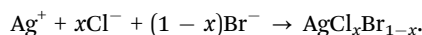
In situ characterization of the synthesis of $\text{AgCl}_x\text{Br}_{1-x}$ nanoparticles was performed in a home-made glass vessel customized at the beamline 1-ID of the Advanced Photon Source (APS) with the use of the high-energy (70 keV, with a wavelength of 0.1771 Å) synchrotron X-ray beam.^{29,30} A schematic illustration of the experimental set-up is shown in Fig. 1, highlighting the working mechanism of the *in situ* setup. The glass reaction vessel was specifically designed with a 5 mm optical path length in the reaction solutions and two parallel flat windows that were large enough to collect the significant scattering signals. When the *in situ* measurements were performed, the incident X-ray beam (300 $\mu\text{m} \times 300 \mu\text{m}$) was aligned to be perpendicular to the windows. The powerful penetration capability of the high-energy, high-flux, synchrotron X-ray beam enabled the sensitive detection of solid nanocrystals in the large-volume reaction solutions. In a typical *in situ* synthesis, the precursor AgNO_3 solution was injected into the reaction solution with the assistance of a programmed syringe pump. Once the injection of AgNO_3 solution started (normalized as 0 s of time), the optical shutter was simultaneously opened to allow the X-ray beam to probe the reaction products in the solution. The corresponding XRD patterns were continuously recorded using a GE 41RT area detector and the interval between two sequential XRD patterns was 1 second. The two-dimensional diffraction patterns were calibrated using a standard LaB_6 powder dispersed in ethanol and converted to 1D plots using Fit2D software.³¹ The background was determined by measuring the X-ray scattering from the ethylene glycol solution of PVP with the same concentration as the reaction solution and was subtracted from all the XRD patterns obtained during the reaction. For quantitative analysis, the most intensive $\text{AgCl}_x\text{Br}_{1-x}$ (200) peaks were fitted with the Gaussian function and the extracted peak intensity and peak position were used to follow the nucleation and growth events involved in the formation of $\text{AgCl}_x\text{Br}_{1-x}$ nanocubes. In addition, the chemical composition of the final product was determined using the crystalline lattice constant (a) according to Vegard's law,³²

$$a_{\text{AgCl}_x\text{Br}_{1-x}} = x \times a_{\text{AgCl}} + (1-x) \times a_{\text{AgBr}}$$

Meanwhile, the full-width at half-maximum (FWHM) of these XRD peaks was analyzed and the Scherrer equation was employed to estimate the crystallite size. The detailed method is described in the ESI† (Fig. S1 and S2, and the corresponding description).

3 Results and discussion

Nanocubes made of silver chlorobromide ($\text{AgCl}_x\text{Br}_{1-x}$, $0 < x < 1$) have been successfully synthesized *via* a recently developed co-precipitation strategy in viscous solution:



The reaction kinetics between the Ag^+ ions and the mixed halogen ions (*i.e.*, Cl^- and Br^-) are sensitive toward the reaction temperature, which can slightly influence the size of nanocubes, and the injection rate of the precursor AgNO_3 solution, which can significantly influence the morphology, the size, the composition, and the phase purity of the products. Therefore, we focus on understanding the reaction kinetics involved in the synthesis of $\text{AgCl}_x\text{Br}_{1-x}$ nanoparticles as a function of the injection rate of the precursor AgNO_3 solution by applying the time-resolved high-energy synchrotron XRD technique (Fig. 1) to follow the co-precipitation reactions in real time.

Although the average composition (*i.e.*, the value of x) of the synthesized $\text{AgCl}_x\text{Br}_{1-x}$ nanoparticles can be easily tuned by controlling the ratio of different halogen anions in the reaction solutions, only the syntheses performed with solutions containing KBr and NaCl at a $[\text{Cl}^-]/[\text{Br}^-]$ ratio of 1 : 1 have been studied to evaluate the influence of the injection rate of the precursor AgNO_3 solution due to the limited available beam time. In the first *in situ* synthesis, 1 mL of AgNO_3 solution is added to the reaction solution at an injection rate of 1 mL min^{-1} and the corresponding XRD patterns of the reaction solution are simultaneously collected at different times. The time-resolved XRD patterns are plotted in Fig. 2. No diffraction signals of nanocrystals are detected even after the precursor AgNO_3 solution has been completely injected into the reaction solution (*i.e.*, at 60 s), indicating that the formation of solid nanocrystalline nuclei from the homogeneous solution containing both Ag^+ cations and halogen anions takes time. Clear diffraction signals start to appear at $t = 65 \text{ s}$, *i.e.*, 5 s after the complete addition of the AgNO_3 solution. The intensity of XRD peaks increases quickly with the reaction time. The diffraction peaks are symmetric and they can be assigned to (200) and (220) reflections of the face-centred cubic lattice of $\text{AgCl}_x\text{Br}_{1-x}$ nanocrystals. The positions of the diffraction peaks remain essentially unchanged during the reaction, corresponding to that the $\text{AgCl}_x\text{Br}_{1-x}$ nanocrystals continuously grow the stable seeds with the same composition determined by the nuclei (Fig. 3A). The final composition of the synthesized nanoparticles was calculated to be $\text{AgCl}_{0.44}\text{Br}_{0.56}$ according to Vegard's law. The ratio of $[\text{Cl}^-]/[\text{Br}^-]$ is 0.44/0.56 (*i.e.*, 0.79), which is apparently less than the ratio of $[\text{Cl}^-]/[\text{Br}^-]$ in the reaction solution (*i.e.*, 1).

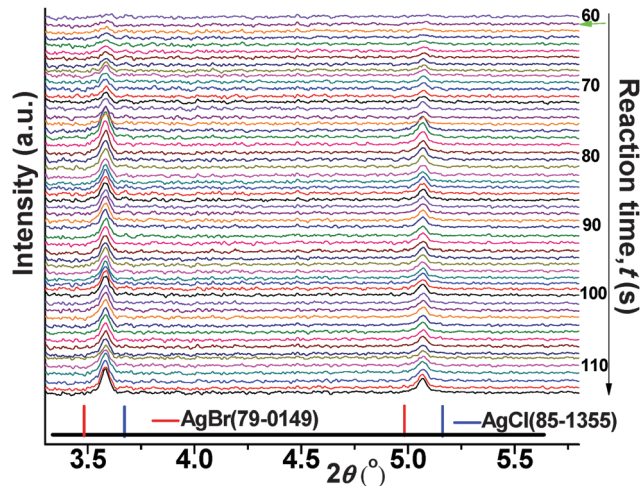


Fig. 2 Time-resolved XRD patterns recorded from the reaction solution containing KBr and NaCl (with the molar ratio $([\text{Cl}^-]/[\text{Br}^-]) = 1 : 1$) and AgNO_3 that was added at an injection rate of 1 mL min^{-1} . The wavelength of X-ray was 0.1771 \AA . The XRD peaks at low and high angles correspond to (200) and (220) reflections of $\text{AgCl}_x\text{Br}_{1-x}$ nanocrystals. (Green arrow highlights the time at which $\text{AgCl}_x\text{Br}_{1-x}$ nanocrystals start to be detected.)

The difference indicates that the co-precipitation reaction tends to form silver halide nuclei with more Br^- ions in a closed system, which is consistent with a lower solubility product of AgBr compared to AgCl.³³

The peak area of a XRD pattern is proportional to the mass of the corresponding crystalline material when its crystalline phase is constant. As a result, the time-dependent evolution of the peak area can be used to represent the reaction kinetics regarding the mass change of $\text{AgCl}_x\text{Br}_{1-x}$ nanocrystals during the synthesis. Fig. 3B presents the change in the peak area of the $\text{AgCl}_{0.44}\text{Br}_{0.56}$ (200) peak (*i.e.*, the first peak in Fig. 2) as a function of the reaction time. Since each $\text{AgCl}_{0.44}\text{Br}_{0.56}$ nanoparticle is a single crystal, the particle size can be represented by the crystallite size that can be estimated from the peak width of XRD peaks with the use of the Scherrer equation. The full-width at half-maximum (FWHM) of the diffraction peaks is extracted from the measured XRD patterns recorded from the reaction solution in the course of synthesis. With subtraction of the instrumental contribution to the peak broadening, the calibrated FWHM is used to calculate the nanoparticle size according to the Scherrer equation. The variation of the particle size as a function of reaction time is plotted in Fig. 3C.

The synthesis can be divided into three stages for convenient analysis and discussion. In region I (*i.e.*, $t = 0\text{--}60 \text{ s}$), the injection of 1 mL of the precursor AgNO_3 solution to the reaction solution dominates. No apparent diffraction peaks of $\text{AgCl}_x\text{Br}_{1-x}$ nanocrystals are observed although the concentration product of free Ag^+ and free halogen ions is much larger than the solubility product constant of either AgCl or AgBr, indicating that the reaction kinetics for the formation of $\text{AgCl}_x\text{Br}_{1-x}$ nanocrystalline nuclei in ethylene glycol is significantly slowed down compared to the precipitation reaction in water. The slowed reaction rate is consistent with that no signal could be discerned even at 60 s (ESI† Fig. S3). In region II

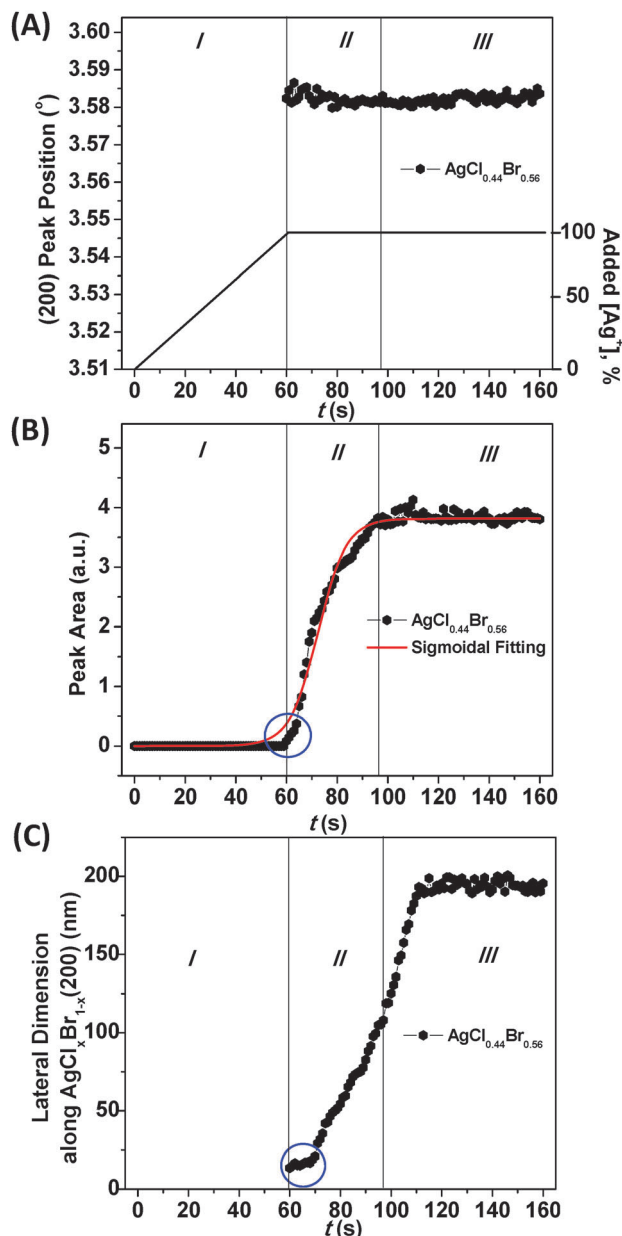


Fig. 3 Evolution of the (A) peak position, (B) peak area of the (200) peak (*i.e.*, the first peak in Fig. 2) and (C) average particle size of $\text{AgCl}_x\text{Br}_{1-x}$ nanocrystals as a function of the reaction time. Vertical lines were added to highlight three distinguished stages involved in the formation of $\text{AgCl}_{0.44}\text{Br}_{0.56}$ nanocrystals. The red curve represents the sigmoidal fitting of the experimental data. The blue oval highlights the difference between the fitting and experimental data that correspond to the nucleation stage.

(*i.e.*, $t = 61\text{--}96$ s), no more precursor AgNO_3 solution is added to the reaction solution. At 61 s, the major (200) peak of $\text{AgCl}_x\text{Br}_{1-x}$ nanocrystals becomes barely identifiable. Both (200) and (220) peaks are well developed and exhibit symmetric profiles as the reaction proceeds to 65 s (Fig. S1, ESI†). At the reaction stage, the average size of the $\text{AgCl}_{0.44}\text{Br}_{0.56}$ particles is estimated to be ~ 15 nm and remains unchanged (highlighted by the blue oval in Fig. 3C) although the peak area slightly increases, indicating that the nucleation process results in the formation of uniform seeds.

A further continuous reaction results in a quick increase in the peak area, indicating the fast growth of $\text{AgCl}_{0.44}\text{Br}_{0.56}$ nanocrystals. The increase stops at ~ 96 s, at which the concentrations of free Ag^+ and halogen anions become too low to support the continuous precipitation reaction. The trajectory of the fast reaction at $t > 65$ s can be fitted with a sigmoid function (*i.e.*, the red curve in Fig. 3B and Table S1, ESI†), indicating that the fast nanocrystal growth follows the typical self-catalytic mechanism.³⁴ The deviation (highlighted by the blue oval in Fig. 3B), *i.e.*, the measured peak area being lower than the fitted sigmoid function, at $t \leq 65$ s indicates that the formation of crystalline $\text{AgCl}_{0.44}\text{Br}_{0.56}$ nuclei (or stable seeds), from which $\text{AgCl}_{0.44}\text{Br}_{0.56}$ nanoparticles with controlled sizes are grown, follows a reaction kinetics slower than the self-catalytic growth process. The difference in reaction kinetics at different reaction stages enables the well separation of nucleation and growth, benefiting the formation of uniform $\text{AgCl}_{0.44}\text{Br}_{0.56}$ nanoparticles. In region III (*i.e.*, $t > 96$ s), the peak area remains constant as a plateau, indicating the completion of the precipitation reaction. Given that the peak area is linearly proportional to the mass of highly crystalline materials, the mass conversion to the $\text{AgCl}_x\text{Br}_{1-x}$ nanoparticles can be calculated as a function of reaction time (Fig. S4, ESI†). In contrast, the average crystalline size of the nanoparticles monotonically increases from 101 nm (@96 s) to 194 nm (@110 s), and then the size remains constant (Fig. 3C). The observed increase in the average size and the consistency in the diffraction peak area (corresponding to the amount of material) together clearly indicate the occurrence of Ostwald ripening during the period of 96–110 s, which is responsible for narrowing down the size distribution of $\text{AgCl}_{0.44}\text{Br}_{0.56}$ nanoparticles. Fig. 4 shows a typical scanning electron microscope (SEM) image of the $\text{AgCl}_{0.44}\text{Br}_{0.56}$ nanoparticles synthesized from the reaction presented in Fig. 3, clearly displaying their high uniformity in terms of size and morphology. These nanoparticles exhibit well-defined cubic morphology and an average size of 190 nm, which agrees well with the crystalline size estimated from the XRD patterns. In all, the *in situ* and *ex situ* characterization results show that the reaction driven by injecting the precursor AgNO_3 solution at a rate of 1 mL min^{-1} can produce high-quality $\text{AgCl}_x\text{Br}_{1-x}$ nanocubes with uniform size and shape as well as well-defined pure composition and crystallinity. In addition, increasing the injection rate of the precursor AgNO_3 solution can always result in the production of uniform $\text{AgCl}_x\text{Br}_{1-x}$ nanocubes similar to the quality of those shown in Fig. 4 except the size.²⁷ The similarity in high quality of the $\text{AgCl}_x\text{Br}_{1-x}$ nanocubes synthesized at injection rates larger than 1 mL min^{-1} indicates that uniform nanocubes can be synthesized by completely adding the precursor AgNO_3 solution to the reaction solution before the nucleation process starts. The uniformity of the $\text{AgCl}_x\text{Br}_{1-x}$ nanocubes is beneficial for assembling them into ordered superlattices (inset, Fig. 4), such as three-dimensional ordered photonic bandgap crystals.²⁷

In contrast, lowering the injection rate of the precursor AgNO_3 solution leads to a significant influence on the quality of $\text{AgCl}_x\text{Br}_{1-x}$ nanocrystals. The effect has been evaluated *in situ*

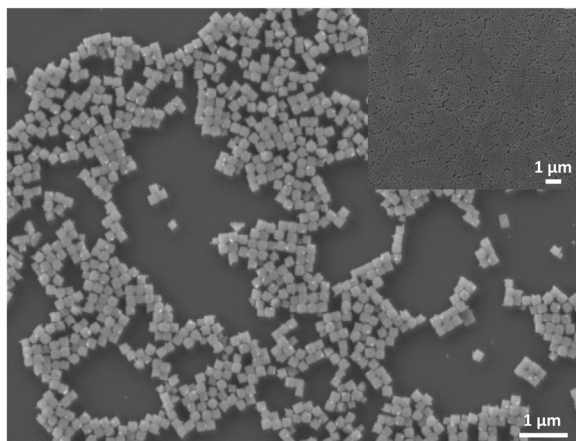


Fig. 4 Typical SEM image of uniform $\text{AgCl}_{0.44}\text{Br}_{0.56}$ nanocubes synthesized through the reaction shown in Fig. 3.

by following the reaction performed with an injection rate of AgNO_3 solution at 0.2 mL min^{-1} . With this low injection rate, it takes 300 s to completely add 1 mL of precursor AgNO_3 solution to the reaction solution. Once the injection of the AgNO_3 solution starts (*i.e.*, the moment being recorded as $t = 0$ s), the XRD pattern of the reaction solution is continuously recorded with a time interval of 1 s.

The time-resolved XRD patterns are presented in Fig. 5. Similar to the reaction shown in Fig. 2, it takes a period of time (*i.e.*, ~ 140 s during which 47% AgNO_3 solution has been added to the reaction solution) to observe the appearance of XRD signals of $\text{AgCl}_x\text{Br}_{1-x}$ nanocrystals. The long-period absence of $\text{AgCl}_x\text{Br}_{1-x}$ nanocrystals in the reaction solution containing both Ag^+ cations and halogen anions again confirms that the formation of $\text{AgCl}_x\text{Br}_{1-x}$ through the precipitation reaction is a slow process. Once the diffraction peaks appear, their intensity increases quickly along with a slight shift of the peak position

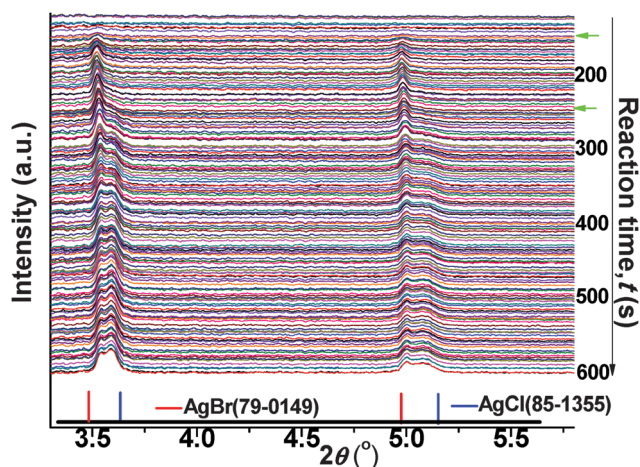


Fig. 5 Time-resolved XRD patterns recorded from the reaction solution containing KBr and NaCl (with the molar ratio $[\text{Cl}^-]/[\text{Br}^-] = 1:1$) and AgNO_3 that was added at an injection rate of 0.2 mL min^{-1} . Other conditions were the same as in Fig. 2. (Green arrows highlight the times at which different types of $\text{AgCl}_x\text{Br}_{1-x}$ nanocrystals start to be detected.)

toward larger diffraction angles. The diffraction peaks become significantly broader at ~ 240 s. A careful analysis of the individual XRD patterns (Fig. S5, ESI†) reveals that the peak broadening is attributed to the formation of new types of $\text{AgCl}_x\text{Br}_{1-x}$ nanocrystals with different compositions rather than an enlargement of the existing nanocrystals, which usually leads to narrowing of XRD peaks. As more AgNO_3 solution is added and the reaction proceeds, the diffraction intensity of both types of $\text{AgCl}_x\text{Br}_{1-x}$ nanocrystals gradually increases, while that of the second type of $\text{AgCl}_x\text{Br}_{1-x}$ nanocrystals increases faster. For convenience, the $\text{AgCl}_x\text{Br}_{1-x}$ nanocrystals with XRD peaks at lower 2θ are labelled as Type-I $\text{AgCl}_x\text{Br}_{1-x}$ (*i.e.*, the firstly formed $\text{AgCl}_x\text{Br}_{1-x}$ nanocrystalline phase) and those with XRD peaks at higher 2θ as Type-II $\text{AgCl}_x\text{Br}_{1-x}$ (*i.e.*, the secondly formed $\text{AgCl}_x\text{Br}_{1-x}$ nanocrystalline phase) in the following discussion.

The reaction product formed during the period of 140–240 s contains only the Type-I $\text{AgCl}_x\text{Br}_{1-x}$ nanocrystals. The quantitative information on the diffraction peaks including the peak position and the peak area can be directly extracted as the data shown in Fig. 3. However, the product formed at $t > 240$ s is a mixture of both Type-I and Type-II $\text{AgCl}_x\text{Br}_{1-x}$ nanocrystals. Deconvolution of the two crystalline phases is realized by fitting the overlapped diffraction peaks with Gaussian functions, leading to the determination of the peak positions and the peak areas of both $\text{AgCl}_x\text{Br}_{1-x}$ phases (Fig. S5, ESI†). The evolution of the peak position and the peak area of the (200) diffraction peaks of both Type-I and Type-II $\text{AgCl}_x\text{Br}_{1-x}$ nanocrystals is presented in Fig. 6A and B, respectively, as a function of the reaction time. In this reaction, more AgNO_3 solution is continuously injected into the reaction solution after the formation of $\text{AgCl}_x\text{Br}_{1-x}$ nanocrystals is initiated, which is different from the reaction shown in Fig. 3. This synthesis can be divided into four stages for convenient analysis and discussion. In region I (*i.e.*, $t = 0$ –140 s), no detectable XRD signals of $\text{AgCl}_x\text{Br}_{1-x}$ nanocrystals is observed before 47% of the precursor AgNO_3 solution has been added to the reaction solution. The longer time (*i.e.*, 140 s *versus* 60 s) required to initiate the formation of $\text{AgCl}_x\text{Br}_{1-x}$ nanocrystals compared with the experiment shown in Fig. 3 indicates that the slow nucleation process involved in the formation of $\text{AgCl}_x\text{Br}_{1-x}$ nanocrystals also depends on the concentration of the precursor Ag^+ ion. In region II (*i.e.*, $t = 140$ –240 s), the formation of only Type-I $\text{AgCl}_x\text{Br}_{1-x}$ nanocrystals is detected (Fig. 6, red filled circles). In the period of 140–200 s, the mass of Type-I $\text{AgCl}_x\text{Br}_{1-x}$ nanocrystals increases dramatically, while the peak position remains essentially constant at $2\theta = 3.525^\circ$ (corresponding to $\text{AgCl}_{0.02}\text{Br}_{0.98}$). The corresponding reaction kinetics is similar to that shown in Fig. 3. The as-formed $\text{AgCl}_x\text{Br}_{1-x}$ nanocrystals have a much lower concentration of Cl^- ions compared with the $\text{AgCl}_x\text{Br}_{1-x}$ nanocrystals shown in Fig. 4, further confirming that Ag^+ ions prefer to precipitate with Br^- ions when the concentration of free Ag^+ ions is lower than that of the free halogen ions. The preferential precipitation of Ag^+ with Br^- quickly lowers the concentration of free Br^- in the reaction solution, resulting in an increased ratio of $[\text{Cl}^-]/[\text{Br}^-]$ in solution. At $t > 200$ s, the increase of the peak area becomes much slower, but the peak position gradually shifts to higher diffraction

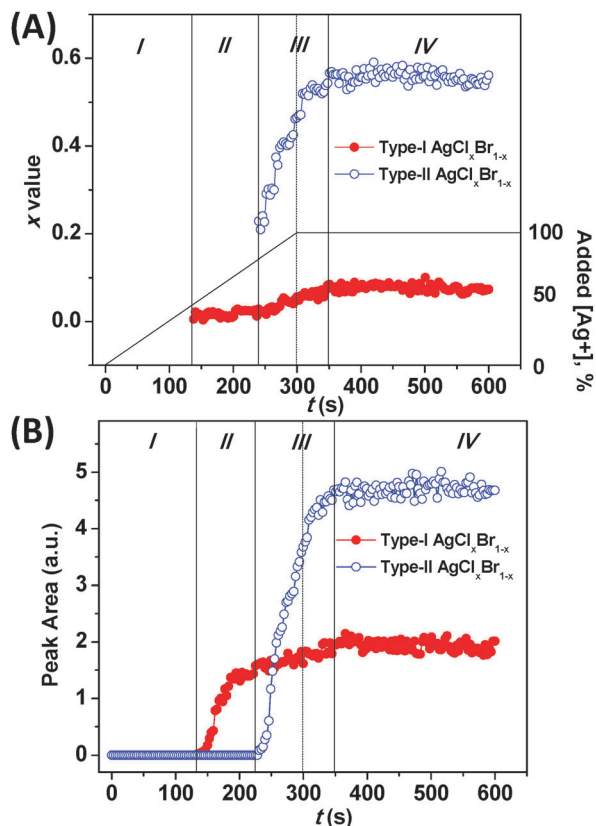


Fig. 6 Evolution of the (A) x value in $\text{AgCl}_x\text{Br}_{1-x}$, (B) peak area of the $\text{AgCl}_x\text{Br}_{1-x}$ (200) peaks (*i.e.*, the first group of peaks in Fig. 5) as a function of the reaction time. Vertical lines were added to highlight four distinguished stages involved in the formation of two different types of $\text{AgCl}_x\text{Br}_{1-x}$ nanocrystals.

angles. According to Bragg's law (*i.e.*, $2d \sin \theta = \lambda$) and Vegard's law, the $\text{AgCl}_x\text{Br}_{1-x}$ nanocrystals with the peak position at a smaller angle have a larger interplanar distance (d), corresponding to a higher concentration of Br^- in the $\text{AgCl}_x\text{Br}_{1-x}$ nanocrystals. The peak shifting from smaller angles to higher angles indicates the compositional variation of Type-I $\text{AgCl}_x\text{Br}_{1-x}$ nanocrystals with an increase in the average concentration of Cl^- in the nanocrystals. This trend continues even after a new phase of Type-II $\text{AgCl}_x\text{Br}_{1-x}$ nanocrystals appears in the reaction solution. The slow increase in the mass and peak shifting to large diffraction angles of Type-I $\text{AgCl}_x\text{Br}_{1-x}$ nanocrystals indicate that the bromide-enriched $\text{AgCl}_{0.02}\text{Br}_{0.98}$ nanocrystals formed at the early stage are overgrown with $\text{AgCl}_x\text{Br}_{1-x}$ containing more Cl^- followed by alloying in the reaction solution. As the precipitation reaction proceeds along with more addition of AgNO_3 , the ratio of $[\text{Cl}^-]/[\text{Br}^-]$ in the reaction solution becomes higher and higher, which triggers the formation of Type-II $\text{AgCl}_x\text{Br}_{1-x}$ nanocrystals with much more Cl^- at ~ 240 s. In region III (*i.e.*, $t = 240\text{--}350$ s), in addition to the slight compositional variation of Type-I $\text{AgCl}_x\text{Br}_{1-x}$ nanocrystals, nucleation and growth of Type-II $\text{AgCl}_x\text{Br}_{1-x}$ nanocrystals becomes the dominating process in this time period. At 240 s, when 80% of the precursor AgNO_3 solution has been added to the reaction solution, XRD signals of Type-II $\text{AgCl}_x\text{Br}_{1-x}$ nanocrystals start to

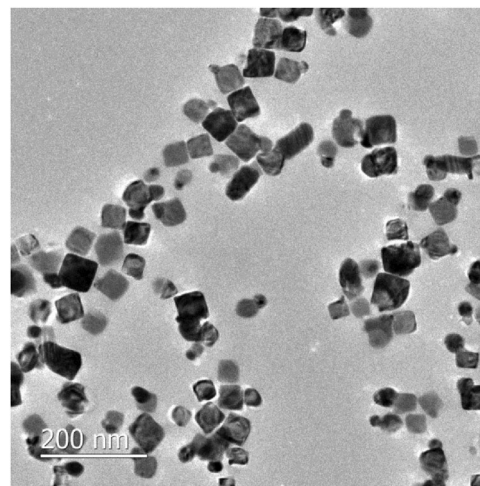


Fig. 7 TEM image of the $\text{AgCl}_x\text{Br}_{1-x}$ nanoparticles synthesized from the reaction shown in Fig. 6.

be observed. In the following 110 s, the corresponding peak area quickly increases to reach a plateau at $t > 350$ s. Meanwhile the (200) peak position also gradually shifts from 3.555° to 3.591° (corresponding to nanocrystals with compositions from $\text{AgCl}_{0.23}\text{Br}_{0.77}$ to $\text{AgCl}_{0.57}\text{Br}_{0.43}$). Similarly, the XRD signals of Type-I $\text{AgCl}_x\text{Br}_{1-x}$ nanocrystals also become stable with a composition of $\text{AgCl}_{0.07}\text{Br}_{0.93}$. In region IV (*i.e.*, $t > 350$ s), the (200) peak area and the peak position of both Type-I and Type-II $\text{AgCl}_x\text{Br}_{1-x}$ nanocrystals exhibit plateaus, indicating that the termination of precipitation reactions shuts down variation of both types of nanocrystals at the same time. Apparently this synthesis involves multiple nucleation processes that are not beneficial for the formation of uniform nanoparticles.³⁵ Fig. 7 presents a typical transmission electron microscope (TEM) image of the final product containing both $\text{AgCl}_{0.07}\text{Br}_{0.93}$ and $\text{AgCl}_{0.57}\text{Br}_{0.43}$ nanocrystals. The sizes of the nanoparticles broadly distribute from 10 nm to 80 nm. Although most particles exhibit cubic morphology, there are still many particles with various morphologies including sphere, rod, dimer, *etc.* The apparent difference in nanoparticles shown in Fig. 4 and 7 directly confirms the importance of the injection rate of the precursor AgNO_3 solution in determining the quality of $\text{AgCl}_x\text{Br}_{1-x}$ nanocrystals.

4 Conclusions

Silver chlorobromide nanoparticles can be synthesized through a co-precipitation reaction between Ag^+ cations and mixed halogen anions (*i.e.*, Cl^- and Br^-) by injecting an ethylene glycol solution of AgNO_3 into an ethylene glycol solution containing both Cl^- and Br^- . *In situ* high-energy synchrotron X-ray diffraction has been used to probe the reaction kinetics by monitoring the variation of the peak area and the peak position in the course of nanoparticle formation. The *in situ* studies reveal that the reactions driven by injecting AgNO_3 solution at different rates (1 mL min^{-1} versus 0.2 mL min^{-1}) follows

significantly different reaction kinetics (including both nucleation and growth processes), which are responsible for different qualities of the resulting $\text{AgCl}_x\text{Br}_{1-x}$ nanoparticles. With a high injection rate ($\geq 1 \text{ mL min}^{-1}$), the precursor AgNO_3 can be completely added to the reaction solution before the nucleation process starts. This condition leads to the good separation of nucleation and growth steps in a closed reaction system, which benefits the formation of uniform nanocubes with well-defined composition and narrow size distribution. In contrast, with the low injection rate (e.g., 0.2 mL min^{-1}), more AgNO_3 solution is continuously added to the reaction solution after nucleation of $\text{AgCl}_x\text{Br}_{1-x}$ nanocrystals starts, leading to continuous multiple nucleation/growth processes. This situation cannot well separate nucleation and growth steps, resulting in the formation of $\text{AgCl}_x\text{Br}_{1-x}$ nanoparticles with broad distributions. The quantitative analysis of *in situ* results indicates that the reaction kinetics can be controlled by varying the injection rate of the precursor AgNO_3 solution to improve uniformity of the $\text{AgCl}_x\text{Br}_{1-x}$ nanoparticles. The difference in the products formed from the two reactions at different injection rates of the precursor AgNO_3 solution further highlights the importance of kinetic-control rather than thermodynamic-control in determining the quality of nanoparticles. It is believed that the *in situ* high-energy synchrotron X-ray diffraction represents a powerful technique to study reaction kinetics involved in the synthesis of many other interesting nanocrystals. The real-time information is helpful to optimize the reaction conditions to improve the quality of nanocrystals.

Acknowledgements

The use of the Center for Nanoscale Materials was granted by the U.S. Department of Energy, Office of Science, Office of Basic Energy Sciences, under Contract No. DE-AC02-06CH11357. This research used resources of the Advanced Photon Source, a U.S. Department of Energy (DOE) Office of Science User Facility operated for the DOE Office of Science by Argonne National Laboratory under Contract No. DE-AC02-06CH11357.

Notes and references

- 1 C. An, S. Peng and Y. Sun, *Adv. Mater.*, 2010, **22**, 2570–2574.
- 2 C. An, J. Wang, J. Liu, S. Wang and Y. Sun, *ChemSusChem*, 2013, **6**, 1931–1937.
- 3 C. An, J. Wang, S. Wang, Q. Zhang, M. Yang and J. Zhan, *CrystEngComm*, 2012, **14**, 5886–5891.
- 4 P. Hu, X. Hu, C. Chen, D. Hou and Y. Huang, *CrystEngComm*, 2014, **16**, 649–653.
- 5 J. Jiang and L. Zhang, *Chem. – Eur. J.*, 2011, **17**, 3710–3717.
- 6 Y. Sun, *J. Phys. Chem. C*, 2010, **114**, 2127–2133.
- 7 P. Wang, B. Huang, X. Qin, X. Zhang, Y. Dai, J. Wei and M.-H. Whangbo, *Angew. Chem., Int. Ed.*, 2008, **47**, 7931–7933.
- 8 P. Wang, B. Huang, X. Zhang, X. Qin, H. Jin, Y. Dai, Z. Wang, J. Wei, J. Zhan, S. Wang, J. Wang and M.-H. Whangbo, *Chem. – Eur. J.*, 2009, **15**, 1821–1824.
- 9 L. Ye, J. Liu, C. Gong, L. Tian, T. Peng and L. Zan, *ACS Catal.*, 2012, **2**, 1677–1683.
- 10 L. Kuai, B. Geng, X. Chen, Y. Zhao and Y. Luo, *Langmuir*, 2010, **26**, 18723–18727.
- 11 H. Xu, H. Li, J. Xia, S. Yin, Z. Luo, L. Liu and L. Xu, *ACS Appl. Mater. Interfaces*, 2010, **3**, 22–29.
- 12 H. Zhang, X. Fan, X. Quan, S. Chen and H. Yu, *Environ. Sci. Technol.*, 2011, **45**, 5731–5736.
- 13 S. Glaus and G. Calzaferri, *Photochem. Photobiol. Sci.*, 2003, **2**, 398–401.
- 14 R. Dong, B. Tian, C. Zeng, T. Li, T. Wang and J. Zhang, *J. Phys. Chem. C*, 2012, **117**, 213–220.
- 15 S. Wu, X. Shen, Z. Ji, G. Zhu, C. Chen, K. Chen, R. Bu and L. Yang, *CrystEngComm*, 2015, **17**, 2517–2522.
- 16 B.-Z. Dekel and A. Katzir, *Appl. Opt.*, 2005, **44**, 3343–3348.
- 17 P. Ephrat, K. Roodenko, L. Nagli and A. Katzir, *Appl. Phys. Lett.*, 2004, **84**, 637–639.
- 18 T. Lewi, S. Shalem, A. Tsun and A. Katzir, *Appl. Phys. Lett.*, 2007, **91**, 251112.
- 19 E. Rave, L. Nagli and A. Katzir, *Opt. Lett.*, 2000, **25**, 1237–1239.
- 20 X. Ma, Y. Dai, M. Guo and B. Huang, *ChemPhysChem*, 2012, **13**, 2304–2309.
- 21 Y. Bi and J. Ye, *Chem. – Eur. J.*, 2010, **16**, 10327–10331.
- 22 M. Choi, K.-H. Shin and J. Jang, *J. Colloid Interface Sci.*, 2010, **341**, 83–87.
- 23 N. Kakuta, N. Goto, H. Ohkita and T. Mizushima, *J. Phys. Chem. B*, 1999, **103**, 5917–5919.
- 24 P. Wang, B. Huang, X. Zhang, X. Qin, Y. Dai, Z. Wang and Z. Lou, *ChemCatChem*, 2011, **3**, 360–364.
- 25 Z. Li and Y. Sun, *J. Mater. Chem. A*, 2013, **1**, 6786–6793.
- 26 B. Cai, J. Wang, D. Han, S. Gan, Q. Zhang, Z. Wu and L. Niu, *Nanoscale*, 2013, **5**, 10989–10995.
- 27 Z. Li, J. S. Okasinski, D. J. Gosztola, Y. Ren and Y. Sun, *J. Mater. Chem. C*, 2015, **3**, 58–65.
- 28 Y. Sun and Y. Ren, *Part. Part. Syst. Charact.*, 2013, **30**, 399–419.
- 29 S. Peng, J. S. Okasinski, J. D. Almer, Y. Ren, L. Wang, W. Yang and Y. Sun, *J. Phys. Chem. C*, 2012, **116**, 11842–11847.
- 30 Z. Li, J. S. Okasinski, J. D. Almer, Y. Ren, X. Zuo and Y. Sun, *Nanoscale*, 2014, **6**, 365–370.
- 31 A. Hammersley, S. Svensson, M. Hanfland, A. Fitch and D. Hausermann, *High Pressure Res.*, 1996, **14**, 235–248.
- 32 R. S. Eachus, A. P. Marchetti and A. A. Muentner, *Annu. Rev. Phys. Chem.*, 1999, **50**, 117–144.
- 33 H. Trimble, *Ind. Eng. Chem.*, 1931, **23**, 165–167.
- 34 Y. Chen, X. Cui, K. Zhang, D. Pan, S. Zhang, B. Wang and J. Hou, *Chem. Phys. Lett.*, 2003, **369**, 16–20.
- 35 C. H. Bamford and C. F. H. Tipper, *Comprehensive chemical kinetics*, Elsevier scientific, Amsterdam, section 8, vol. 22, 1980.